Control Engineering Practice 16 (2008) 1509–1518

Contents lists available at ScienceDirect

Control Engineering Practice

journal homepage: www.elsevier.com/locate/conengprac

Kalman filter configurations for a low-cost loosely integrated inertial navigation system on an airship

Johan Bijker, Willem Steyn *

Department of Electrical & Electronic Engineering, University of Stellenbosch, PBag X1, Matieland 7602, South Africa

ARTICLE INFO

Article history:
Received 14 December 2007
Accepted 29 April 2008
Available online 24 June 2008

Keywords:
Airship
Inertial navigation
Extended kalman filter
Position and attitude estimation

ABSTRACT

A comparative study of various Kalman filter configurations applied to a low-cost inertial navigation system (INS) for an unmanned airship or blimp was made. The attitude of the airship was determined using micro-electromechanical sensors (MEMS) gyros with feedback from the earth's magnetic field and gravity vectors. MEMS accelerometer measurements were used as a gravity vector, as the dynamic accelerations on an airship are small compared with the static gravitational acceleration. The velocity and position estimates were updated from a loosely integrated GPS receiver. It was found that the best trade-off between accuracy and processing power could be achieved by having two smaller extended Kalman filters (EKF) running in sequence. The first EKF estimates the attitude of the airship, while the second EKF estimates the velocity and position of the airship. The solution was implemented on an onboard computer to provide real-time navigation estimates.

1. Introduction

During the early 1980s, advantages of unmanned airships or blimps were rediscovered and used for a variety of tasks, including surveillance, advertising, aerial photography, monitoring and research (Jex, Hogue, & Gelhausen, 1985; Boschma, 1993). More recently, there has been a tremendous interest in controllable unmanned airships as aerial inspection platforms due to their stability properties (Elves, Bueno, Bergerman, & Ramos, 1998; Elves, Bergerman, & Bueno, 2001; Kantor, Wettergreen, Ostrowski, & Singh, 2001; Hima & Bestaoui, 2002; Khoury & Gillett, 1999; Wells, 1995; Wimmer & Well, 2001).

Advances in micro-electromechanical sensors (MEMS) have led to significant developments in low-cost inertial technology in the last decade (Barbour & Schmidt, 2001). Because of the ongoing development, these sensors are improving (reductions in size, weight and sensitivity) and becoming cheaper due to mass production. However, the drawback is that MEMS are not yet able to reach the types of accuracies obtainable from traditional technologies (Hide, Moore, & Smith, 2004). Without a GPS receiver, the sensors used in an inertial navigation system (INS) had to be very accurate and stable to ensure good navigation results over a long period of time. With the integration of GPS and INS, the navigation errors are always kept within a certain range, because GPS measurement errors are not a function of time. The integration is normally done in an extended Kalman filter (EKF) and various applications have been reported in the literature, e.g. Alcocer, Oliviera, and Pascoal (2007) on the positioning of an autonomous underwater vehicle and Koifman and Merhav (1991) on the attitude reference system of an aircraft.

For practical measurements and implementation of the INS, a relatively small-tethered blimp (4 m in length) as shown in Fig. 1 was used. It was filled with helium to provide the buoyant force.

2. Flight dynamics

To determine typical flight dynamics for the tethered blimp, various test flights were conducted with all sensors on board. The IMU was build for less than $1k US using Analog Devices' ADXL203 MEMS accelerometers and ADXRS401 MEMS rate sensors. The earth's magnetic field was measured with Honeywell's HMC2003 magneto-resistive vector magnetometer. An uBlox Antaris GPS receiver was used to provide position and velocity information.

The magnitude of the accelerations, angular rates and North/East/Down (NED) velocities during a test flight are shown in Figs. 2–4, respectively. The height of the blimp is included to show that during free flight the blimp experiences much lower accelerations and angular rates as and when the tethered blimp is launched or retrieved.

From Fig. 2, the tethered blimp can experience accelerations in the order of 2 m/s^2 during launch and recovery, but peaking only around 0.4 m/s^2 during free flight. The static acceleration (gravity)

* Corresponding author. Tel.: +27 21 8084926; fax: +27 21 8084981.
E-mail address: whsteyn@sun.ac.za (W. Steyn).

0967-0661/$ - see front matter © 2008 Elsevier Ltd. All rights reserved.
doi:10.1016/j.conengprac.2008.04.011

Fig. 1. Tethered blimp used for test flights.

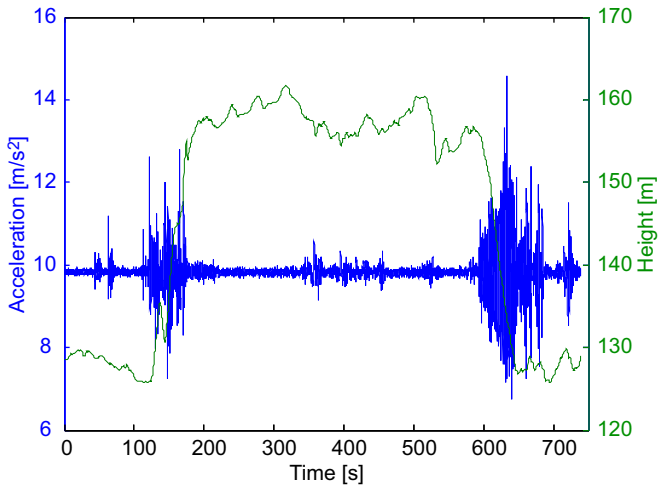

Fig. 2. Magnitude of the accelerometer measurements during a test flight.

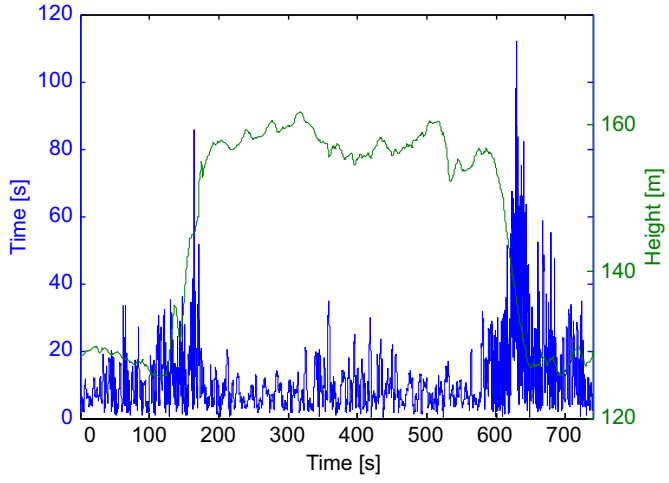

Fig. 3. Magnitude of the gyro measurements during a test flight.

of 9.81 m/s^2 can clearly be seen. Because of the small dynamic accelerations during free flight, the accelerometer measurements can be used as a noisy gravity vector.

Referring to Fig. 3, the angular rates stay mostly below 20° per second during free flight. However, during launch and recovery, the turn rates can exceed 80° per second.

The NED velocities of the blimp are shown in Fig. 4. During free flight, the velocities stay usually below 2 m/s, oscillating with a period of 20–25 s. The Down velocity gives a good indication of the change in height of the blimp.

3. Dynamic equations

3.1. Attitude

For a singularity-free attitude representation, the quaternion was used. The quaternion multiplication scheme that was used differs from historical multiplication conventions. See Lefferts, Markley, and Shuster (1982) and Markley (2003) for a complete discussion. The quaternion dynamic equation can be expressed as

$$\dot{\mathbf{q}} = \frac{1}{2}\boldsymbol{\omega} \otimes \mathbf{q} \tag{1}$$

where $\mathbf{q}$ is the attitude quaternion, $\boldsymbol{\omega}$ is a quaternion formed from the body angular rates (NED referenced) and the $\otimes$ operator implies quaternion multiplication.

3.2. Bias drifts

The gyro model given in Lefferts et al. (1982) includes a bias drift. The bias drift can be approximated by the following model:

$$\dot{\vec{\mathbf{b}}} = \vec{\boldsymbol{\eta}}_{gb} \tag{2}$$

where $\vec{\mathbf{b}}$ is the gyro bias vector and $\vec{\boldsymbol{\eta}}_{gb}$ is a Gaussian zero mean white-noise vector.

3.3. Velocity and position

For a slow-moving blimp travelling-limited distances, the earth can be modelled as perfectly round and non-rotating. The dynamics of the ECEF geocentric longitude, latitude and height in terms of NED velocities are (Titterton & Weston, 1997):

$$\dot{\varphi} = \frac{V_E}{(R+h)\cos\lambda} \tag{3}$$

$$\dot{\lambda} = \frac{V_N}{R+h} \tag{4}$$

$$\dot{h} = -V_D \tag{5}$$

where φ is the longitude (E/W), λ is the latitude (N/S), h is the height above the earth, R is the earth's radius and V is the velocity in NED coordinates.

Because MEMS accelerometers measures dynamic accelerations combined with static acceleration (gravity of the earth), the gravity must be removed before the accelerations can be integrated to obtain velocity. When gravity is assumed to be −9.81 m/s^2 downwards and $\mathbf{A}(\mathbf{q})$ is the direction cosine matrix in terms of a quaternion between the NED axial system and the body axial system of the blimp, the dynamic equations of the NED velocities are:

$$\dot{\mathbf{V}}_{\mathrm{NED}} = \begin{bmatrix} 0 & 0 & 9.81 \end{bmatrix}^{\mathrm{T}} + \mathbf{A}^{\mathrm{T}}(\mathbf{q})\,\vec{\mathbf{f}} \tag{6}$$

where $\vec{\mathbf{f}}$ contains the accelerometer measurements in body axes. This simple gravity model was sufficient for this application using low-cost MEMS sensors.

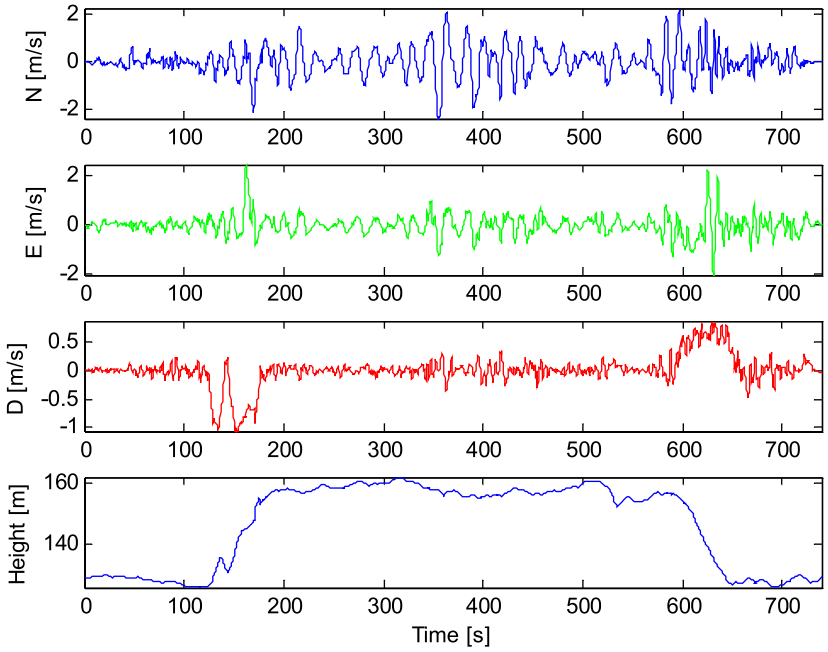

Fig. 4. GPS velocities during a test flight.

3.4. Quaternion perturbation states

In the multiplicative EKF (MEKF), the error between the real $\mathbf{q}$ and the estimated $\hat{\mathbf{q}}$ quaternion is defined as an error quaternion $\boldsymbol{\delta}\mathbf{q}$ with which the estimated quaternion must be multiplied to obtain the true quaternion (Markley, 2003). The primary reason for using an error quaternion is that the unity constraint of the quaternion will be met when using quaternion multiplication. In mathematical terms it can be expressed as

$$\mathbf{q} = \boldsymbol{\delta}\mathbf{q} \otimes \hat{\mathbf{q}} \tag{7}$$

If the error quaternion denotes a small rotation, the scalar part of the error quaternion will be close to one, and the only dynamics of the system will be contained in the vector part of the perturbation quaternion. From Lefferts et al. (1982), the dynamic equation of the vector part of the error quaternion is

$$\dot{\boldsymbol{\delta}}\vec{\mathbf{q}} = -\vec{\boldsymbol{\omega}} \times \boldsymbol{\delta}\vec{\mathbf{q}} + \frac{1}{2}(-\boldsymbol{\delta}\vec{\mathbf{b}} - \vec{\boldsymbol{\eta}}_{gm}) \tag{8}$$

where $\boldsymbol{\delta}\vec{\mathbf{b}}$ contains the bias perturbations and $\vec{\boldsymbol{\eta}}_{gm}$ is the gyro measurement noise.

From (7), the estimated quaternion can be corrected with the error quaternion vector to give the true (or state estimation updated/corrected) quaternion, as

$$\begin{bmatrix} q_1 \\ q_2 \\ q_3 \\ q_4 \end{bmatrix} = \begin{bmatrix} \hat{q}_4 & -\hat{q}_3 & \hat{q}_2 \\ \hat{q}_3 & \hat{q}_4 & -\hat{q}_1 \\ -\hat{q}_2 & \hat{q}_1 & \hat{q}_4 \\ -\hat{q}_1 & -\hat{q}_2 & -\hat{q}_3 \end{bmatrix} \begin{bmatrix} \delta q_1 \\ \delta q_2 \\ \delta q_3 \end{bmatrix} + \begin{bmatrix} \hat{q}_1 \\ \hat{q}_2 \\ \hat{q}_3 \\ \hat{q}_4 \end{bmatrix} \tag{9}$$

A measurement model used in an attitude filter can make use of sensor (e.g. magnetometer) vector pairs, where a measured vector $\vec{\mathbf{v}}^{b}$ in body axes is related to a modelled vector $\vec{\mathbf{v}}^{r}$ in the reference NED axes, as

$$\vec{\mathbf{v}}^{b} = \mathbf{A}(\mathbf{q})\vec{\mathbf{v}}^{r} \tag{10}$$

From Markley (2003) and using (7), the direction cosine matrix can be written as

$$\mathbf{A}(\mathbf{q}) = \mathbf{A}(\boldsymbol{\delta}\mathbf{q} \otimes \hat{\mathbf{q}}) = \mathbf{A}(\boldsymbol{\delta}\mathbf{q})\mathbf{A}(\hat{\mathbf{q}}) \tag{11}$$

Therefore, from (10) and (11), the measured body vector can be written in terms of the estimated body vector $\hat{\vec{\mathbf{v}}}^{b}$ as

$$\vec{\mathbf{v}}^{b} = \mathbf{A}(\boldsymbol{\delta}\mathbf{q})\mathbf{A}(\hat{\mathbf{q}})\vec{\mathbf{v}}^{r} = \mathbf{A}(\boldsymbol{\delta}\mathbf{q})\hat{\vec{\mathbf{v}}}^{b}. \tag{12}$$

For a measurement update on the vector part of the error quaternion, the direction cosine matrix in terms of the estimated quaternion must be constructed to transform a vector in NED axes to an estimated vector in body axes. This estimated body vector can be compared to the measured body vector in order to calculate the error quaternion. More than one vector is needed, because a vector contains only two attitude parameters. As attitude is determined by three independent parameters, at least two vectors are needed (Psiaki, 1990). The magnetic and gravity vectors were used for attitude determination on the blimp.

The direction cosine matrix for a small-error quaternion can be approximated by

$$\mathbf{A}(\boldsymbol{\delta}\mathbf{q}) \approx \begin{bmatrix} 1 & 2\delta q_3 & -2\delta q_2 \\ -2\delta q_3 & 1 & 2\delta q_1 \\ 2\delta q_2 & -2\delta q_1 & 1 \end{bmatrix}. \tag{13}$$

Per vector measurement, the output error $\mathbf{e}$ (filter innovation) in terms of the error quaternion vector is therefore given by

$$\mathbf{e} = \vec{\mathbf{v}}^{b} - \hat{\vec{\mathbf{v}}}^{b} = 2\hat{\vec{\mathbf{v}}}^{b} \times \boldsymbol{\delta}\vec{\mathbf{q}} \tag{14}$$

3.5. Velocity perturbation states

Rewriting (6) in terms of the estimated quaternion, and including noise from the accelerometers

$$\dot{\hat{\mathbf{V}}}_{\mathrm{NED}} = \begin{bmatrix} 0 & 0 & 9.81 \end{bmatrix}^{\mathrm{T}} + \mathbf{A}^{\mathrm{T}}(\hat{\mathbf{q}})(\vec{\mathbf{f}} + \vec{\boldsymbol{\eta}}_{fm}) \tag{15}$$

where $\vec{\boldsymbol{\eta}}_{fm}$ is accelerometer measurement noise.

Using (6), (11), (13) and (15) the velocity perturbation dynamics can therefore be written as

$$\dot{\boldsymbol{\delta}}\dot{\mathbf{V}}_{\mathrm{NED}} = \dot{\mathbf{V}}_{\mathrm{NED}} - \dot{\hat{\mathbf{V}}}_{\mathrm{NED}} = 2\mathbf{A}^{\mathrm{T}}(\hat{\mathbf{q}})\vec{\mathbf{f}} \times \boldsymbol{\delta}\vec{\mathbf{q}} - \mathbf{A}^{\mathrm{T}}(\hat{\mathbf{q}})\vec{\boldsymbol{\eta}}_{fm}. \tag{16}$$

3.6. Position perturbation states

Using the superposition principle, the longitude, latitude and height perturbation dynamics from (3) to (5) can be written as

$$\delta\dot{\varphi} = \frac{1}{(R+h)\cos\lambda}\delta V_E + \frac{V_E \sin\lambda}{(R+h)\cos^2\lambda}\delta\lambda - \frac{V_E}{(R+h)^2\cos\lambda}\delta h \tag{17}$$

$$\delta\dot{\lambda} = \frac{1}{R+h}\delta V_N - \frac{V_N}{(R+h)^2}\delta h \tag{18}$$

$$\delta\dot{h} = -\delta h. \tag{19}$$

4. Extended Kalman filter

The continuous perturbation equations presented above can be implemented in an EKF. For a discrete implementation in an onboard computer, the perturbation dynamic equations must be converted to the discrete domain. In the early days of autonomous flight linear-fixed-gain Kalman filters, based on a linearised model of the aircraft in straight-and-level flight, was used. However, substantial errors in attitude estimation was experienced and it was soon realised that a variable-gain EKF is necessary (Koifman & Merhav, 1991). Two different filtering approaches are discussed below:

(1) All the perturbation dynamic equations will be used to form one big EKF.
(2) The problem is split into two: one EKF will estimate the attitude of the blimp, while a second EKF will estimate the velocity and position vector of the blimp.

4.1. Big EKF

A 12 perturbation state EKF can be constructed by using (8), (16)–(19). As the quaternion perturbation (error) vector can be used to update the full quaternion vector, 13 states will be estimated using the accelerometer and gyro inputs. Noise couples into the system via gyro measurement noise, gyro bias drift noise and accelerometer measurement noise. The maximum expected accelerometer bias drift noise will make contributions less than the GPS position errors over GPS outage periods of under 15 s and was not estimated in this application. The complete perturbation state-space model of the EKF is given, as

$$\begin{bmatrix} \delta\dot{q}_1 \\ \delta\dot{q}_2 \\ \delta\dot{q}_3 \\ \delta\dot{b}_x \\ \delta\dot{b}_y \\ \delta\dot{b}_z \\ \delta\dot{V}_n \\ \delta\dot{V}_e \\ \delta\dot{V}_d \\ \delta\dot{\varphi} \\ \delta\dot{\lambda} \\ \delta\dot{h} \end{bmatrix} = \left[\begin{array}{ccc:ccc:ccc:ccc} 0 & \omega_3 & -\omega_2 & -0.5 & 0 & 0 & 0 & 0 & 0 & 0 & 0 & 0 \\ -\omega_3 & 0 & \omega_1 & 0 & -0.5 & 0 & 0 & 0 & 0 & 0 & 0 & 0 \\ \omega_2 & -\omega_1 & 0 & 0 & 0 & -0.5 & 0 & 0 & 0 & 0 & 0 & 0 \\ \hdashline 0 & 0 & 0 & 0 & 0 & 0 & 0 & 0 & 0 & 0 & 0 & 0 \\ 0 & 0 & 0 & 0 & 0 & 0 & 0 & 0 & 0 & 0 & 0 & 0 \\ 0 & 0 & 0 & 0 & 0 & 0 & 0 & 0 & 0 & 0 & 0 & 0 \\ \hdashline \multicolumn{3}{c:}{\multirow{3}{*}{$\mathbf{A}^{\mathrm{T}}\,\hat{\mathbf{q}}\begin{bmatrix} 0 & -2f_z & 2f_y \\ 2f_z & 0 & -2f_x \\ -2f_y & 2f_x & 0 \end{bmatrix}$}} & 0 & 0 & 0 & 0 & 0 & 0 & 0 & 0 & 0 \\ & & & 0 & 0 & 0 & 0 & 0 & 0 & 0 & 0 & 0 \\ & & & 0 & 0 & 0 & 0 & 0 & 0 & 0 & 0 & 0 \\ \hdashline 0 & 0 & 0 & 0 & 0 & 0 & 0 & \frac{1}{R+h\cos\lambda} & 0 & 0 & \frac{V_E \sin\lambda}{R+h\cos^2\lambda} & \frac{-V_E}{R+h^2\cos\lambda} \\ 0 & 0 & 0 & 0 & 0 & 0 & \frac{1}{R+h} & 0 & 0 & 0 & 0 & \frac{-V_N}{R+h^2} \\ 0 & 0 & 0 & 0 & 0 & 0 & 0 & 0 & -1 & 0 & 0 & 0 \end{array}\right] \times \begin{bmatrix} \delta q_1 \\ \delta q_2 \\ \delta q_3 \\ \delta b_x \\ \delta b_y \\ \delta b_z \\ \delta V_n \\ \delta V_e \\ \delta V_d \\ \delta\varphi \\ \delta\lambda \\ \delta h \end{bmatrix} + \left[\begin{array}{ccc:ccc:ccc} -0.5 & 0 & 0 & 0 & 0 & 0 & 0 & 0 & 0 \\ 0 & -0.5 & 0 & 0 & 0 & 0 & 0 & 0 & 0 \\ 0 & 0 & -0.5 & 0 & 0 & 0 & 0 & 0 & 0 \\ \hdashline 0 & 0 & 0 & 1 & 0 & 0 & 0 & 0 & 0 \\ 0 & 0 & 0 & 0 & 1 & 0 & 0 & 0 & 0 \\ 0 & 0 & 0 & 0 & 0 & 1 & 0 & 0 & 0 \\ \hdashline 0 & 0 & 0 & 0 & 0 & 0 & \multicolumn{3}{c:}{\multirow{3}{*}{$-\mathbf{A}^{\mathrm{T}}\,\hat{\mathbf{q}}$}} \\ 0 & 0 & 0 & 0 & 0 & 0 & & & \\ 0 & 0 & 0 & 0 & 0 & 0 & & & \\ \hdashline 0 & 0 & 0 & 0 & 0 & 0 & 0 & 0 & 0 \\ 0 & 0 & 0 & 0 & 0 & 0 & 0 & 0 & 0 \\ 0 & 0 & 0 & 0 & 0 & 0 & 0 & 0 & 0 \end{array}\right] \begin{bmatrix} \eta_{gmx} \\ \eta_{gmy} \\ \eta_{gmz} \\ \eta_{gbx} \\ \eta_{gby} \\ \eta_{gbz} \\ \eta_{fmx} \\ \eta_{fmy} \\ \eta_{fmz} \end{bmatrix} \tag{20}$$

The vector part of the attitude error quaternion can be updated by using (14), while the velocity and position states can be updated directly by GPS measurements

$$\begin{bmatrix} V_N & V_E & V_D & \varphi & \lambda & h \end{bmatrix}^{\mathrm{T}} = \begin{bmatrix} \hat{V}_N & \hat{V}_E & \hat{V}_D & \hat{\varphi} & \hat{\lambda} & \hat{h} \end{bmatrix}^{\mathrm{T}} + \begin{bmatrix} \delta V_N & \delta V_E & \delta V_D & \delta\varphi & \delta\lambda & \delta h \end{bmatrix}^{\mathrm{T}} \tag{21}$$

However, the GPS velocity updates also contain attitude information, which eliminates the use of the accelerometers as a gravity vector sensor. The EKF states are still completely observable when using only one type of vector measurement in (14), combined with the GPS measurements in (21). For a general airship implementation (during periods of low horizontal velocity), when the body experience unrestricted accelerations caused by wind turbulence, the gravity vector measurement will present large errors to the EKF. The magnetometer measurements can then be still used to have fully observable EKF states.

4.2. Two smaller EKFs

The attitude of the blimp can be estimated by using the dynamic perturbation model of (8) in an EKF. Six perturbation states are estimated using the gyro inputs: three for the quaternion vector perturbations, and three for the gyro bias perturbations. Noise couples into the system via gyro measurement noise and gyro bias drift noise. The perturbation state-space kinematic model of the attitude EKF, is

$$\begin{bmatrix}\delta\dot{q}_1\\ \delta\dot{q}_2\\ \delta\dot{q}_3\\ \delta\dot{b}_1\\ \delta\dot{b}_2\\ \delta\dot{b}_3\end{bmatrix}=\begin{bmatrix}0 & \omega_3 & -\omega_2 & -0.5 & 0 & 0\\ -\omega_3 & 0 & \omega_1 & 0 & -0.5 & 0\\ \omega_2 & -\omega_1 & 0 & 0 & 0 & -0.5\\ 0 & 0 & 0 & 0 & 0 & 0\\ 0 & 0 & 0 & 0 & 0 & 0\\ 0 & 0 & 0 & 0 & 0 & 0\end{bmatrix}\begin{bmatrix}\delta q_1\\ \delta q_2\\ \delta q_3\\ \delta b_1\\ \delta b_2\\ \delta b_3\end{bmatrix}+\begin{bmatrix}-0.5 & 0 & 0 & 0 & 0 & 0\\ 0 & -0.5 & 0 & 0 & 0 & 0\\ 0 & 0 & -0.5 & 0 & 0 & 0\\ 0 & 0 & 0 & 1 & 0 & 0\\ 0 & 0 & 0 & 0 & 1 & 0\\ 0 & 0 & 0 & 0 & 0 & 1\end{bmatrix}\begin{bmatrix}\eta_{gmx}\\ \eta_{gmy}\\ \eta_{gmz}\\ \eta_{gbx}\\ \eta_{gby}\\ \eta_{gbz}\end{bmatrix}. \tag{22}$$

The measurement matrix given in (14) can be used for both the magnetic and gravity vector updates. Both vectors are needed in this case for complete observability.

The velocity and position can be estimated by combining (16)–(19) in a position EKF. Six perturbation states are estimated using three accelerometer measurements. Noise couples into the system via accelerometer measurement noise and quaternion estimation noise. The perturbation state-space dynamics model of the position EKF, is

$$\begin{bmatrix}\delta\dot{\varphi}\\ \delta\dot{\lambda}\\ \delta\dot{h}\\ \delta\dot{V}_N\\ \delta\dot{V}_E\\ \delta\dot{V}_D\end{bmatrix}=\begin{bmatrix}0 & \frac{V_E\sin\lambda}{(R+h)\cos^2\lambda} & \frac{-V_E}{(R+h)^2\cos\lambda} & 0 & \frac{1}{(R+h)\cos\lambda} & 0\\ 0 & 0 & \frac{-V_N}{(R+h)^2} & \frac{1}{R+h} & 0 & 0\\ 0 & 0 & 0 & 0 & 0 & -1\\ 0 & 0 & 0 & 0 & 0 & 0\\ 0 & 0 & 0 & 0 & 0 & 0\\ 0 & 0 & 0 & 0 & 0 & 0\end{bmatrix}\begin{bmatrix}\delta\varphi\\ \delta\lambda\\ \delta h\\ \delta V_N\\ \delta V_E\\ \delta V_D\end{bmatrix}+\begin{bmatrix}0 & 0 & 0\\ 0 & 0 & 0\\ 0 & 0 & 0\\ -\mathbf{A}^{\mathrm{T}}\end{bmatrix}\begin{bmatrix}\eta_{fmx}\\ \eta_{fmy}\\ \eta_{fmz}\end{bmatrix}$$
$$+2\begin{bmatrix}0 & 0 & 0 & 0\\ 0 & 0 & 0 & 0\\ 0 & 0 & 0 & 0\\ q_1f_x+q_2f_y+q_3f_z & -q_2f_x+q_1f_y+q_4f_z & -q_3f_x-q_4f_y+q_1f_z & q_4f_x-q_3f_y+q_2f_z\\ q_2f_x-q_1f_y-q_4f_z & q_1f_x+q_2f_y+q_3f_z & q_4f_x-q_3f_y+q_2f_z & q_3f_x+q_4f_y-q_1f_z\\ q_3f_x+q_4f_y-q_1f_z & -q_4f_x+q_3f_y-q_2f_z & q_1f_x+q_2f_y+q_3f_z & -q_2f_x+q_1f_y+q_4f_z\end{bmatrix}\begin{bmatrix}\eta_{q1}\\ \eta_{q2}\\ \eta_{q3}\\ \eta_{q4}\end{bmatrix} \tag{23}$$

where $\boldsymbol{\eta}_q$ is the noise on the quaternion estimates.

Eq. (21) can be used directly as the measurement model, because all six states can be updated by the GPS receiver.

4.3. EKF matrix equations and processing power

A discrete implementation of the EKF is given below. The matrix $\boldsymbol{\Phi}$ is the discrete equivalent of the continuous-perturbated state transition matrix, $\mathbf{H}$ is the linearised innovation output matrix of the discrete non-linear measurement model, $\mathbf{M}$ and $\mathbf{P}$ are the pre- and postupdate covariance matrix of the state errors, $\mathbf{Q}$ is the covariance matrix of the discrete process noise and $\mathbf{R}$ is the constant covariance matrix of the discrete measurement noise.

(1) State propagation (numerical integration of non-linear continuous state model):

$$\overline{\mathbf{x}}(k+1)=\hat{\mathbf{x}}(k)+\int_k^{k+1}\mathbf{f}_k(\hat{\mathbf{x}}(k),k)\,\mathrm{d}t. \tag{24}$$

(2) Increase in noise figures of the propagated states:

$$\mathbf{M}(k+1)=\boldsymbol{\Phi}(k)\mathbf{P}(k)\boldsymbol{\Phi}(k)^{\mathrm{T}}+\mathbf{Q}(k). \tag{25}$$

If there are measurement updates available, the error between the propagated and measured outputs could be used to correct the model as defined below.

(3) Calculation of the optimal estimator update gain:

$$\mathbf{K}(k+1)=\mathbf{M}(k+1)\mathbf{H}(k)^{\mathrm{T}}[\mathbf{H}(k)\mathbf{M}(k+1)\mathbf{H}(k)^{\mathrm{T}}+\mathbf{R}]^{-1} \tag{26}$$

(4) State update:

$$\hat{\mathbf{x}}(k+1)=\overline{\mathbf{x}}(k+1)+\mathbf{K}(k+1)\mathbf{e}(k+1) \tag{27}$$

where, $\mathbf{e}(k+1)=\overset{-b}{\mathbf{v}}_{\mathrm{meas}}(k+1)-\overset{\wedge b}{\mathbf{v}}_{\mathrm{estim}}(k+1)$ (EKF innovation)

(5) Update of noise figures:

$$\mathbf{P}(k+1)=[\mathbf{I}-\mathbf{K}(k+1)\mathbf{H}(k+1)]\mathbf{M}(k+1)[\mathbf{I}-\mathbf{K}(k+1)\times\mathbf{H}(k+1)]^{\mathrm{T}}+\mathbf{K}(k+1)\mathbf{R}\mathbf{K}(k+1)^{\mathrm{T}}. \tag{28}$$

Table 1
Floating-point operations for matrix calculations

Matrix multiplication	$(n \times m) \times (m \times p)$	$2nmp$
Matrix inversion	$(p \times p)^{-1}$	$2p^3+3p^2+6p-1$

Table 2
Number of FLOPS required for the EKF matrix equations

Equation number	FLOPS
(25)	$4n^3+n^2$
(26)	$2p^3+4p^2+4n^2p+4np^2+6p-1$
(27)	$2np+2p$
(28)	$4n^3+4n^2p+2np^2+n^2$

Defining a floating-point operation (FLOPS) as the addition, subtraction, multiplication or division of two floating-point numbers, the number of FLOPS needed for basic matrix calculations can be calculated. Matrix multiplication was done by using the classical method, meaning no special speed-up algorithms were used. Matrix inversion was done by LU decomposition with forward and back substitution (Press, 1992). See Table 1 for the FLOPS required to do matrix multiplication and inversion.

Assume an EKF has n states (perturbations) and p outputs (measurements). The number of FLOPS for the EKF matrix equations can be calculated and is given in Table 2.

The total number of FLOPS to propagate the EKF covariance, (25), is

$$4n^3 + n^2 \tag{29}$$

The total number of FLOPS during EKF measurement updates, (26)–(28), is

$$4n^3 + n^2(8p + 1) + n(6p^2 + 2p) + 2p^3 + 4p^2 + 8p - 1 \tag{30}$$

Knowing the update rate between measurements and the rate of updates, the number of FLOPS per second can be calculated. The number of FLOPS is a function of the number of states and number of measurements to the power of three, which means a significant increase in computing power for an increase in Kalman filter size. Due to the reasonable sparse nature of the EKF matrices in this application and the diagonal symmetry of **M** and **P**, the FLOPS calculated above can be reduced somewhat by customised software. This was, however, not considered for the EKF processing comparisons below.

5. Simulations

To simulate the various sensor measurements on board, the blimp, the blimp was treated as a point mass. The motion of the point mass was simulated with a six degrees of freedom block in Simulink. Inputs to the block were forces and torques, and the block gave accelerations, velocities, angular accelerations, angular rates and angles (attitude) as output. All the sensors were modelled to simulate real-world effects, including noise, bias random walk, cross coupling and A/D quantisation effects. See Table 3 below for the sensor measurement noise and bias characteristics.

The inputs to the block were set up to represent typical blimp movement. The forces were set up for the blimp to have NED sinusoidal velocities with a period of 20–25 s and magnitudes below 2 m/s (acceleration peaks at 0.4 m/s^2). The torques were set up for the blimp to roll and pitch up to 10°, and to yaw up to 20° with a period of 20–25 s (see Section 8 for practical blimp attitude estimates). All simulations assume:

Table 3
Sensor noise characteristics used in simulations

Sensor	RMS measurement noise	RMS bias noise
GPS position	3 m horizontal	0
	4 m vertical	0
GPS velocity	0.5 m/s all directions	0
Rate sensor	0.185 deg/s	0.021 deg/s/s
Accelerometer	0.036 m/s^2	0.0013 m/s^2/s (0.04 m/s^2 drift max)
Magnetometer	0.035 μT	0.021 μT/s (0.8 μT drift max)

Initial NED location at : $\varphi = 18.86675^\circ, \quad \lambda = -33.92863^\circ, \quad h = 130\,\text{m MSL}$

Local magnetic field vector $= \begin{bmatrix} 9.69974 & -4.32305 & -23.7753 \end{bmatrix}^{\mathrm{T}} \mu\mathrm{T}$

5.1. Solution A

The attitude, velocity and position were estimated by the big EKF given in (20), using the gyro and accelerometer measurements. It has 12 perturbation states, with nine noise inputs (gyro measurement noise, gyro bias drift noise and accelerometer measurement noise). Every 20 ms, the filter is updated with a magnetometer vector, resulting in a measurement matrix of three rows. Every 250 ms, the GPS velocity and position updates are included, resulting in a measurement matrix of nine rows. The filter estimates the attitude, gyro bias drifts, velocity and position of the blimp. This solution is a general-purpose solution with no constraints to the accelerations, the airship may experience. See Fig. 5 for a schematical layout of the filter.

5.2. Solution B

The same Kalman filter was used as in Solution A, but this time the updates were customised for application on an airship where the accelerometers can be used to measure the earth's gravity vector. The accelerometer data is therefore used as an input to the Kalman filter dynamic state equations, as well as a feedback measurement. Every 20 ms, the measurement has six rows, containing the magnetometer vector and gravity vector. Every 250 ms, the GPS velocity and position updates are included, resulting in a measurement matrix of 12 rows.

5.3. Solution C

The attitude is estimated with the attitude EKF estimator given in equation (22), using the gyro measurements. It consists of six perturbation states with six noise inputs (gyro measurement noise and gyro bias drift noise). The measurement matrix has six rows (magnetometer and gravity vectors), every 20 ms. The Kalman filter estimates the attitude of the airship and gyro bias drifts.

The velocity and position is estimated by the position EKF in (23). It uses the accelerometer measurements together with the quaternion estimates of the attitude EKF. This EKF consists of six states, with seven noise inputs (noise on the four quaternion elements and noise on the three accelerometer measurements). All six states are updated by the GPS every 250 ms. The two filters are run in sequence, as shown in Fig. 6.

6. Simulation results

The performance of the three different solutions described above is compared through a Monte Carlo analysis from random initial conditions. A typical result from the same initial condition is presented in Table 4. The RMS errors of the attitude, velocity and position are given as an accuracy indication of the estimates. The number of FLOPS per second is given as an indication of the processing power needed for implementation on a onboard computer.

Comparing solution A and B with solution C, the first significant conclusion is that a big EKF does not always guarantee a significant performance increase. In fact, the big Kalman filters of solutions A and B performed only marginally better for attitude estimation than the two smaller Kalman filters of solution C, while requiring 3–4 times more FLOPS per second.

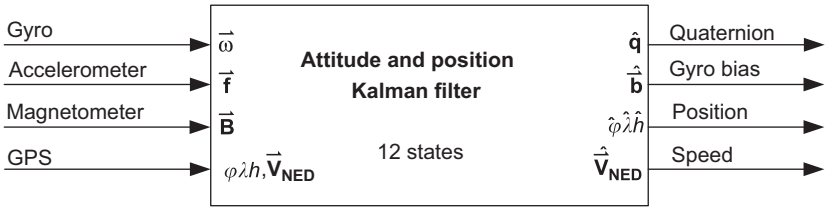

Fig. 5. Combined attitude and position Kalman filter.

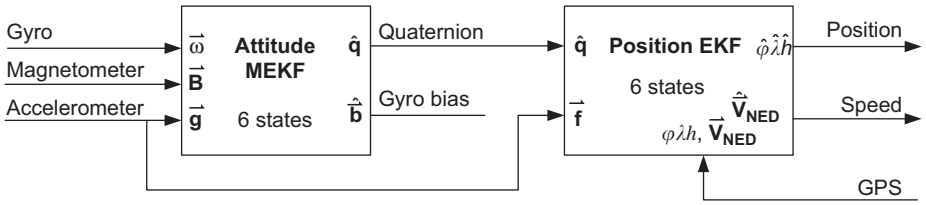

Fig. 6. Attitude Kalman filter in sequence with the position Kalman filter.

Table 4
Comparison of different EKF simulation solutions

Kalman filter solution	States	FLOPS	RMS errors		
			Attitude (deg)	Velocity (m/s)	Position (m)
Solution A	**12**	**975,970**	**1.2228**	**0.3872**	**1.1334**
Solution B	**12**	**1,292,494**	**1.6214**	**0.3996**	**1.1406**
Solution C	**12**	**339,426**	**1.8035**	**0.3994**	**1.1403**
Attitude estimator	6	275,950	1.8035		
Position estimator	6	634,76		0.3994	1.1403

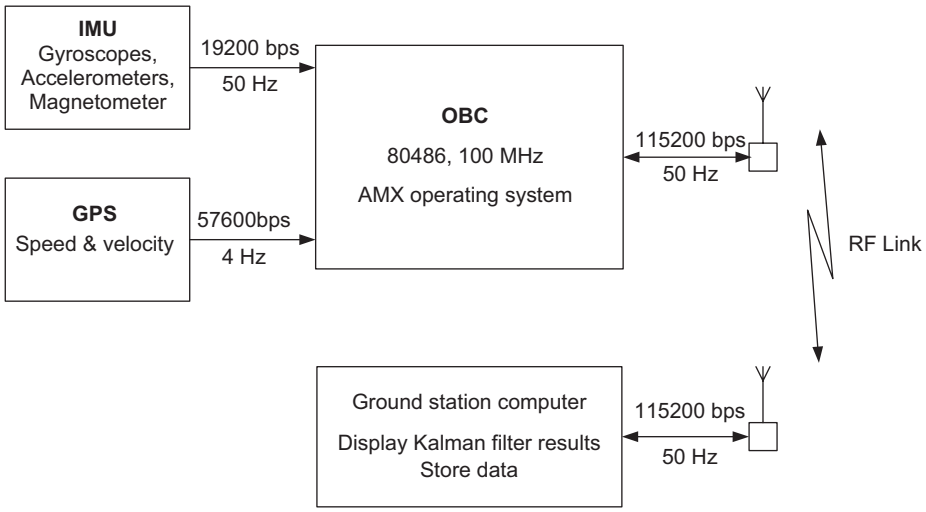

Fig. 7. Schematic layout of the final solution implemented.

However, solution A is usable for all types of vehicles, whereas solution B and C are not. When solution A is customised for use on an airship (as is done in solution B), the bigger Kalman filter of solution B requires about a million more FLOPS per second compared to solution C. This implies that there is a trade-off between a marginal performance improvement and processing power, therefore it is better to split a big Kalman filter into smaller Kalman filters for the blimp/airship application. Solution C gives the best trade-off between accuracy and processing power, and was chosen to be implemented. It should also be considered that the attitude estimator of solution C will still operate optimally even without the availability of GPS updates. GPS updates can be temporarily lost due to the weak reception of satellite signals, which can be caused by a variety of reasons. The other solutions will be significantly affected by the absence of GPS updates.

The simulated RMS noise figures on GPS measurements were 3 m for the horizontal position, 4 m for the vertical position and 0.5 m/s for the NED velocities. A TRIAD (Shuster & Oh, 1981) simulation on the noisy accelerometer and magnetometer measurements, with similar body acceleration disturbances ($0.4\,m/s^2$ peaks), showed a total attitude RMS error of 3.66°. All the solutions above have less noise on the estimated attitude, position and velocity results, illustrating the advantage of combining GPS and INS measurements. Solution A performed marginally better as expected, since it is not using the accelerometers (as disturbed by body motion) to extract attitude information through the gravity vector updates.

Table 5
(EKF–TRIAD) Attitude error during practical test flight

EKF solution	Roll error (deg)	Pitch error (deg)	Yaw error (deg)	Total RMS error (deg)
Solution B	1.83	1.27	3.46	4.12
Solution C	1.82	1.28	3.29	3.97

7. Implementation

Fig. 7 gives a schematic layout of the solution implemented. On board, the blimp are a PC104 OBC, IMU, GPS receiver and RF link. The OBC communicates via a RF link with a ground station computer.

For a real-time implementation of solutions B and C, the Kalman filters were written in C and linked with the AMX 86 real-time operating system (RTOS) to run on the OBC. An RTOS is needed to ensure that all timing-sensitive tasks are executed on time. With an ordinary operating system, housekeeping tasks may prevent the time-sensitive tasks to execute on time. Matrix inversion routines were taken from Press (1992).

The OBC receives the gyroscope, accelerometer and magnetometer outputs every 20 ms from the IMU via a RS232 link operating at 19200 bps. The GPS module provides position and velocity updates every 250 ms via a RS232 link operating at 57600 bps. The sensor and GPS data are packed, time stamped and sent over the RF link to the ground station. All the data is processed onboard with the Kalman filters. The Kalman filter results are sent over the RF link to the ground station. The ground station software displays the IMU data and the Kalman filter results in real-time on a computer screen. In addition, the ground station is used to command the OBC to perform certain tasks, e.g. Kalman filter initialisation, sensor self-test functions, and magnetometer set/reset actions.

8. Practical results

The EKF solutions B and C were implemented in a flight test of about 12 min. During the whole flight, the blimp was anchored with ropes to prevent it from floating away. The blimp was launched about 25 m in the air, where it floated for about 8 min and then pulled back for retrieval.

8.1. Attitude estimation

Fig. 8 shows the attitude estimation of solution C in terms of roll, pitch and yaw angles. It is clear that most of the blimp's

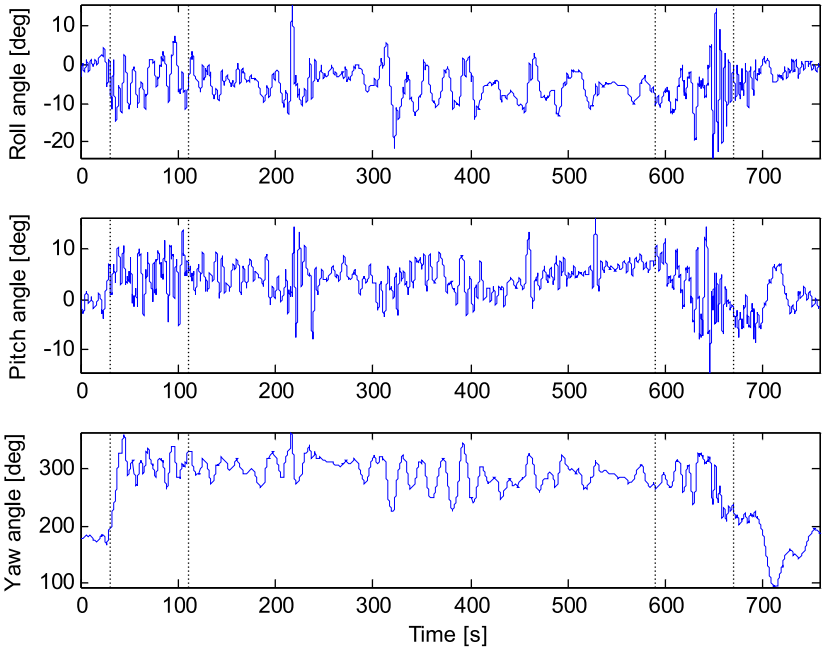

Fig. 8. Attitude estimation in terms of roll, pitch and yaw angles during a test flight.

movement is in the yaw angle. The roll and pitch angles rarely exceed 10° to both sides. This also corresponds to visual observations of the blimp during flight.

The attitude estimator performed as expected during the whole period. Unfortunately, no independent accurate means was available to sense the true attitude, so it was not possible to obtain the true attitude estimation error. The TRIAD method was used to determine the attitude deterministically, using the measured magnetometer and gravity (accelerometer) vector pairs. Table 5 shows the RMS attitude estimation errors of solutions B and C, when compared to the TRIAD result during free-tethered flight. Usually, the largest accelerations are experienced during the launch and retrieval processes, and one can expect the attitude estimator to show larger errors during these times. The launch and retrieval times are indicated with vertical dotted lines in Figs. 8–10.

Solution B and C performed almost similar, although at a significant difference in processing requirement. The attitude errors of Table 5 are much larger as obtained during simulation, although in this case, the estimated attitude is compared to the TRIAD solution and not to the true attitude. During simulation under similar flight conditions, the TRIAD showed a total RMS error of 3.66°. If one assume most of the attitude errors of Table 5 will be contributed by the TRIAD solution, the true expected attitude errors can be much smaller.

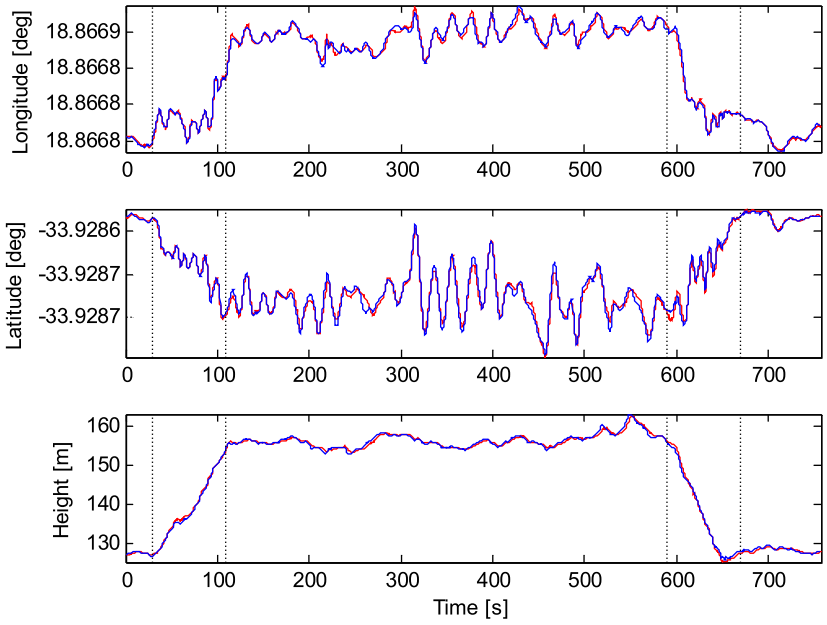

Fig. 9. Position estimates of the blimp during a test flight.

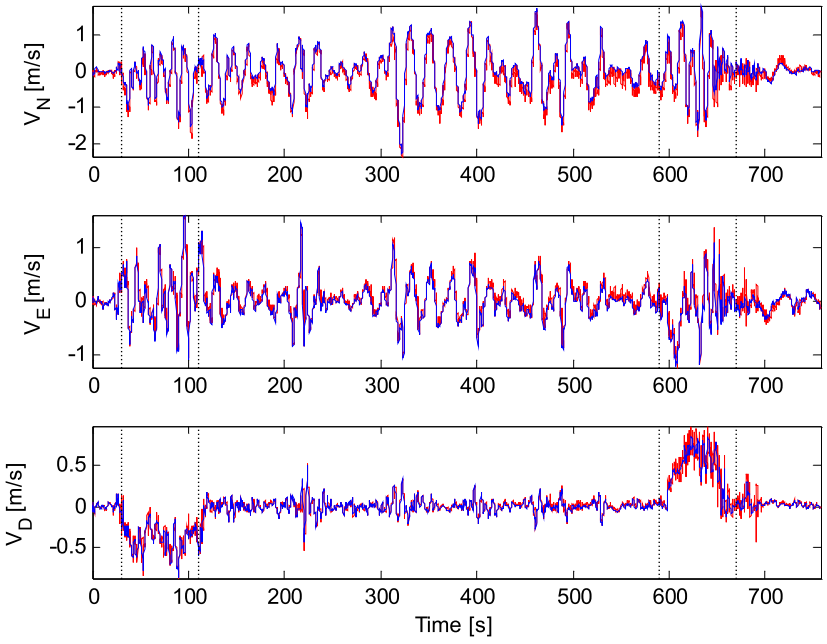

Fig. 10. Velocity estimates of the blimp during a test flight.

8.2. Velocity and position estimation

Fig. 9 provides the position in ECEF geocentric coordinates of the blimp during the test flight (solutions B and C gave similar results). The velocity estimates of the blimp are given in Fig. 10. Blue lines indicate the GPS updates, while red lines indicate the estimated position and velocity. One can see that the GPS updates and Kalman filter estimates fit very well. It signifies that the attitude estimation must be accurate, as the attitude is used to convert accelerations in body axes to NED axes for velocity and position estimation.

As can be seen from Fig. 10, the velocity estimates (red lines) contain more high-speed dynamics compared to the GPS measurements (blue lines). The GPS has a limited bandwidth due to the low update rate and cannot detect all of the blimp's dynamics. The higher-frequency dynamics during the launch (from 30 to 110 s) and retrieval (from 590 to 670 s) can clearly be seen in the velocity estimates. This demonstrates another advantage of using a combination of INS and GPS measurements.

9. Conclusion

A very low-cost attitude and heading reference system for an airship was implemented with an INS made of MEMS devices combined with updates from a GPS receiver. The performance of low cost sensors was enhanced using Kalman filtering. A study of different Kalman filter structures was done, illustrating that only marginally better estimates can be obtained by heavy data processing in a typical large Kalman filter. A trade-off between accuracy and processing power can be made by splitting the estimator in two parts: (1) an attitude estimator and (2) a position estimator.

For application on a slow moving airship, it was shown that the accelerometers of an IMU may be used as a gravity vector measurement, with relevant noise figures applied to compensate for any dynamic acceleration the airship may experience.

References

Alcocer, A., Oliviera, P., & Pascoal, A. (2007). Study and implementation of an EKF GIB-based underwater positioning system. *Control Engineering Practice*, *15*, 689–701.

Barbour, N. M., & Schmidt, G. (2001). Inertial sensor technology trends. *IEEE Sensors Journal*, *1*(4), 332–339.

Boschma, J. H. (1993). The development progress of the US Armys SAA LITE unmanned robot airship. In *10th AIAA lighter-than-air systems technology conference*, Arizona.

Elves, A., Bergerman, M., & Bueno, S. (2001). The potential of robotic airships for planetary exploration. In *10th international conference on advanced robotics,* Budapest, (pp. 131–138).

Elves, A., Bueno, S. S., Bergerman, M., & Ramos, J. J. G. (1998). Project aurora: development of an autonomous unmanned remote monitoring robotic airship. *Journal of the Brazilian Computer Society*, *4*(3).

Hide, C. D., Moore, T., & Smith, M. J. (2004). Multiple model Kalman filtering for GPS and low-cost INS integration. In *Proceedings of ION GNSS*.

Hima, S., & Bestaoui, Y. (2002). Motion generation on trim trajectories for an autonomous underactuated airship. In *Proceedings of the fourth international airship convention & exhibition*.

Jex, H. R., Hogue, J. R., & Gelhausen, P. (1985). Control response measurements of the skyship-500 airship. In *Sixth AIAA lighter-than-air systems technology conference,* Norfolk VA, (pp. 130–141).

Kantor, G., Wettergreen, D., Ostromski, J. P., & Singh, S. (2001). Collection of environmental data from an airship platform. In *Proceedings of the SPIE conference on sensor fusion and decentralized control in robotics systems IV,* Bellingham, WA, (pp. 76–83).

Khoury, G. A., & Gillett, J. D. (1999). *Airship technology, cambridge aerospace series 10*. Cambridge: Cambridge University Press.

Koifman, M., & Merhav, S. J. (1991). Autonomously aided strapdown attitude reference system. *Journal of Guidance, Control, and Dynamics*, *14*(6), 1164–1172.

Lefferts, E. J., Markley, F. L., & Shuster, M. D. (1982). Kalman filtering for spacecraft attitude estimation. *Journal of Guidance, Control, and Dynamics*, *5*(5).

Markley, F. L. (2003). Attitude error representations for Kalman filtering. *Journal of Guidance, Control, and Dynamics*, *26*(2).

Press, W. H. (1992). *Numerical recipes in C: the art of scientific computing* (2nd ed.). Cambridge: Cambridge University Press.

Psiaki, K. L. (1990). Three-axis attitude determination via Kalman filtering of magnetometer data. *Journal of Guidance, Control, and Dynamics*, *13*(3).

Shuster, M. D., & Oh, S. D. (1981). Three-axis attitude determination form vector observations. *Journal of Guidance, Control, and Dynamics*, *4*(1), 70–77.

Titterton, D. H., & Weston, J. L. (1997). Strapdown inertial navigation technology. London: Peter Peregrinus.

Wells, N. (1995). Practical operation of remotely piloted airships. In *11th AIAA lighter-than-air systems technology conference,* Clearwater Beach, FL, (pp. 189-192).

Wimmer, D. -A., & Well, K. H. (2001). Instrumentation, identification and control of airship Lotte. In *14th AIAA lighter-than-air systems technology conference,* Akron Ohio.